Hierarchical Simulations of Diffusion in Zeolites

George K. Papadopoulos, Doros N. Theodorou

School of Chemical Engineering, National Technical University of Athens,
GR 15780 Zografou Campus, Athens, Greece.

Abstract

The work presented in this chapter involves comparison of simulation and experimental results for intracrystalline and long-range diffusion in zeolitic media in order to demonstrate the hierarchical character of the study of transport in microporous structures in response to the need to address sorption and diffusion phenomena in porous materials over broad scales of length and time.

1.   Introduction

The interest in computer studies of diffusion through porous media has grown rapidly over the last two decades, as a result of the advancement of new simulation techniques, force fields and methodologies dealing with the modeling of transport processes at atomistic and mesoscopic scales as well as the development of new central processing unit architectures, which enable computer modeling to be a really powerful tool in diffusion research. The present chapter focuses on transport studies in a special category of nanoporous materials, the zeolites. Their importance in environmental and separation technology as sorbents and catalysts has served as a strong motivation for studying the transport mechanisms of sorbates inside them; moreover, the possibility of tailoring new zeolite structures applicable to specific chemical engineering processes has enhanced the popularity of the field of computer modeling of transport phenomena in porous media.

Previous publications [1-4] in this field have presented extensive reviews of theoretical and experimental aspects of transport in microporous solids in general and zeolites in particular, and have also provided a source of computational methodologies relying on classical and quantum mechanics for use in the atomistic modeling of transport in zeolites. Porous systems under consideration, in the majority of engineering applications, constitute a highly diverse class of materials since their overall structure is characterized by a wide range of length scales. In the next sections of this chapter, special attention is paid to the development of a strategy for studying mass transport in zeolite systems such as catalyst beds or membranes. The diffusion processes are modeled hierarchically from the atomistic scale inside the crystal (0.1 nm) and extending up to the mesoscopic scale of hundreds of crystals and the voids between them (1 mm) in order to

capture the movement of sorbate molecules in the intercrystalline space, in the blocked pores of defect-bearing parts of the medium and over the interfacial regions of the zeolite crystals. In particular, the packing of atoms in the crystal, which form regular lattices of voids varying in width from 0.5 to 10 nm, gives rise to a tensorial anisotropic (depending on the unit cell symmetry) configurational diffusion; in addition, the unavoidable existence of defects in the crystals, introduced during their synthesis procedure, often creates blind pores or secondary macropore networks with a void distribution up to 1 μm or higher, contributing significantly to the effective diffusivity. Moreover, intermediate scale transport phenomena concerning surface diffusion which takes place during adsorption-desorption of the adsorbate molecules on the crystal surface, and molecular or streaming (Knudsen) diffusion in consequence of the intercrystalline fluid mobility, must be rigorously taken into account for the entire modeling of processes such as diffusion, structure-chemical reactions and separations. Therefore, the theoretical and computer simulation approaches to be adopted towards this kind of studies must be capable of addressing sorption and diffusion phenomena over broad scales of length and time in the zeolitic medium.

2. Probing the mass transport mechanism

In section 2.1 below we will discuss selected computer simulation examples at the atomistic scale along with corresponding experimental measurements of diffusivity in silicalite-1 of pure sorbates (carbon dioxide, nitrogen) and a binary mixture (n-butane and methane). The predictions are compared with macroscopic permeation and microscopic quasielastic neutron scattering measurements. Furthermore, in section 2.2 predictions at the mesoscopic scale of the intercrystaline transport of ethane sorbed in beds of NaX zeolite and pulsed field gradient NMR measurements in the same medium over the same length and time scales are compared, in order to investigate the apparent tortuosity factor over the range from Knudsen to molecular diffusion.

2.1 Atomistic scale

2.1.1 Model description

Diffusivity studies at the atomistic scale require modeling of (a) the structure of sorbate molecules and silicalite-1 lattice and (b) the potentials of interaction between atoms or functional groups.

Silicalite-1. Silicalite-1 adopts three crystalline forms, namely the monoclinic with P21/n.1.1 symmetry (mono), the orthorhombic with Pnma symmetry (ortho) and the orthorhombic with P212121 symmetry (para). In highly pure, crystalline silicalite-1 (Si/Al>l000), a reversible monoclinic (P21/n.1.1) – orthorhombic (Pnma) phase transition occurs between 350-363 K [5]. There are three intracrystalline environments where sorbed molecules may reside: interiors of straight channels, interiors of sinusoidal channels, and channel intersections. The interactions of sorbate molecules with the

framework in each of these environments influence their diffusion and adsorption behavior. The results reported here show that N_2 and CO_2 reside preferentially in channel interiors; also, it is shown that silicalite-1 cannot be in its para form under the conditions of the measurements [6].

The coordinates of the atoms in the asymmetric unit of silicalite-1, required for the sorbent potential map calculation, have been taken from ZSM-5 (ortho) and H-ZSM-5 (mono, para) [6] ;   Al was assumed to be completely absent in the calculations.
For the calculation of the Coulombic part of the potential energy (see below), partial charges of −1 and +2, in units of the elementary electronic charge, were placed on oxygen and silicon atoms of the zeolite framework, respectively. These charges are based on semiempirical and local density functional theory electronic embedded cluster calculations [7] and have given satisfactory results in past computations with aromatic molecules in silicalite-1 [8]. Previous simulation works on silicalite-1 have considered the ortho as its prevalent form, except for a few calculations with para [8]. In the present work we have examined the sorption and diffusion of nitrogen by modeling the ortho, para and mono space groups as well.

Sorbates. The diatomic N_2 molecule was modeled as a dumbbell with a rigid interatomic bond. The triatomic linear molecule of CO_2 was modeled using three interaction sites, O, C, O, arranged on a straight line. To describe interactions, a simplified representation was used, cast in terms of Lennard-Jones or Buckingham sites on the atoms and partial charges on the molecular axis; electronic clouds were not considered explicitly. Partial charges were distributed around each molecule so as to reproduce experimental quadrupole moments. (Q_{N2} = - 4.67 × 10^{-40}C m^2 , Q_{CO2} = - 13.67 × 10^{-40} C m^2). The potential energy $V(r)$ used in this work for dispersive interaction is either a 12-6 Lennard-Jones (LJ) potential:

$$V(r) = 4\varepsilon \left[\ (\sigma/r)^{12} - (\sigma/r)^6 \ \right] \tag{1}$$

or an exp 6-1 ''modified'' Buckingham potential (N_2 case), in the sense that $V(r)$ is the sum of a London dispersion-type r^{-6} attractive part taken from LJ, while the repulsive part is an exponential Born-Mayer term:

$$V(r) = A \exp(-br) - 4\varepsilon(\sigma/r)^6 \tag{2}$$

The way zeolite-sorbate interactions were parametrized and computed is described in detail elsewhere [6].
The forces due to partial charges were calculated through the Ewald summation method. The parameter κ determining the width of the Gaussian distribution of charge which screens interactions between neighboring charges in the Ewald method was chosen, so as to make the number of reciprocal space vectors used as small as possible, to keep CPU time low. With this choice of parameters, the direct space term converges within the cutoff distance (minimum image convention). The choices for CO_2, N_2 (3 partial charges) , N_2 (4 partial charges) were respectively ($\kappa = 8 / L_{max}$) , ($\kappa = 8.2 / L_{max}$), ($\kappa = 9 / L_{max}$), where L_{max} is the length of the longest side of our rectangular simulation box.

The sorbate-zeolite electrostatic interactions were calculated based on a pretabulation of the electrostatic potential felt by a test charge at the nodes of a fine cubic mesh constructed throughout the asymmetric unit of silicalite-1. The partial charges attributed to oxygen and silicon atoms of the zeolite framework are reported in Ref. 6 for the various zeolite models used in this work. In most calculations Si atoms were neglected in calculating the non-Coulombic part of the sorbate-sorbent interaction energy. In these calculations we have adopted the values used by June et al. [9] for the L-J parameters of zeolite oxygens; these were obtained by watching computed and experimental values for the Henry's constant of methane at 300 K. Alternatively, we have also adopted the model of Watanabe et al., [10] in which Si atoms are taken explicitly into account in the calculation of the short range terms. These authors obtained optimal parameters for both O and Si by fitting to the experimental Henry's constants for argon, nitrogen and oxygen.

The n-butane molecule is represented in terms of four united-atom methyl and methylene groups (interaction sites). Following June et al. [11], the same potential parameters have been used for both methyl and methylene, although we have assigned the correct masses, 15 and 14 g/mol, respectively, to the two groups. Methane was modeled as a spherical molecule (single interaction site), following Maginn et al. [12]. For the intermolecular interactions between sites on the sorbates (n-butane-n-butane, ethane-methane, n-butane-methane) and for the interaction between sorbates and oxygens of the silicalite-1 crystal, a Lennard-Jones potential was used with a cutoff distance of 13 Å. For n-butane, bond lengths were assumed rigid and constrained to a length of 1.53 Å. Bond angles and torsion angles were allowed to fluctuate under the influence of the following potentials:

$$V_{bend}(\theta) = \frac{1}{2} k_\theta (\theta - \theta_{eq})^2 \tag{3}$$

$$V_{tors}(\phi) = \sum_{k=0}^{5} c_k \cos^k(\phi) \tag{4}$$

The equilibrium value for the bond angle was $\theta_{eq} = 112°$. Values of ε_{ij}, σ_{ij}, k_θ and c_k were identical to those used in Refs 11 and 12. In the pure sorbate cases, these representations have been shown to give predictions for sorption thermodynamics and diffusivity in good agreement with experiment.

2.1.2 Statistical Mechanics of Diffusion

2.1.2.1 Single component systems

In this section the diffusivity results for pure N_2 and CO_2 in silicalite-1 are presented and compared to macroscopic permeability measurements in silicalite-1 membranes and to microscopic QENS experiments in the crystal.

Molecular Dynamics. The dynamical behavior of the system of N_2 and CO_2 in silicalite-1 was studied in the Canonical ensemble (*NVE*), in the absence of any thermodynamic forces that could lead to fluxes within the box. The starting configuration for the equilibrium Molecular Dynamics (MD) simulation was taken from configuration files stored in previous Grand Canonical Monte Carlo simulations for the same temperatures and species [6]. In the MD the particles followed classical trajectories, whose time evolution is governed by Newton's equations of motion; it must be noted that the neglect of quantum effects is fully justified at the temperatures of interest here.

For continuous potentials we need a finite difference approximation of the derivatives to solve the differential equations of motion for the particles. The algorithm chosen for the solution of the differential equations of motion belongs to the category of extrapolation methods, and more specifically to Störmer-leapfrog integrators. Due to its simplicity and exceptional stability, this algorithm affords a long integration time step and low computational cost. Its stability has been attributed to the correspondence between the order of the finite difference equation and its analytical analog, to their time reversibility (algorithm preserves volume in phase space, i.e., is symplectic) and to the oscillating nature of the fundamental solutions (periodicity) [13]. Störmer-leapfrog integrators give fixed time averages and a low drift of the total energy, even with a long integration time step, though they conserve instantaneous total energy rather poorly. Thus, it appears that the trajectory constantly deviates from the initial hypersurface but always finds a way back. Mazur [13] supports the view that the leapfrog scheme is distinguished among the symplectic operators both in terms of the order of truncation errors it produces and the conservation of the total energy it affords, and that the trajectory really manages to sample from a correct hypersurface in phase space with larger step sizes than commonly recommended.

For a linear molecule with fixed internal geometry we would need holonomic constraints introduced into our equations of motion if we were to perform the integration in Cartesian coordinates. However, one of the principal moments of inertia vanishes and the other two are equal. Thus, we can track rotational motion in generalized coordinates using a simple quaternion algorithm with one of the body-fixed angular velocity components (rotation about the molecular axis) being always kept to zero. The total angular velocity and the torque must always be perpendicular to the molecular axis [14]. Fincham has proposed four algorithms as a solution to this problem using a leapfrog scheme [14]; in this work, the LEN algorithm which is recommended by Fincham as superior to the other three (ORT, EXP, IMP) was chosen, since it has the smallest drift energy even for long time-steps. If $\hat{\mathbf{e}}$ is the unit bond vector fixed along the molecule axis, the torque $\mathbf{T}$ on the molecule can be written as

$$\mathbf{T} = \sum_\alpha \mathbf{r}_\alpha \times \mathbf{f}_\alpha = \hat{\mathbf{e}} \times \sum_\alpha d_\alpha \mathbf{f}_\alpha = \hat{\mathbf{e}} \times \mathbf{g} \tag{5}$$

with $\mathbf{g}$ being the "turning force", which can be determined from the nonbonded forces $\mathbf{f}_\alpha$ on each atom, the position vectors $\mathbf{r}_\alpha$ of each interaction site and the (algebraic) distances d_α of each atom α from the centre of mass of the linear molecule. In a linear molecule, $\mathbf{g}$ can be

replaced by its component perpendicular to the molecular axis, $\mathbf{g}_p$, without affecting the torque. $\mathbf{g}_p$ is defined as

$$\mathbf{g}_p = \mathbf{g} - \hat{\mathbf{e}}(\hat{\mathbf{e}} \cdot \mathbf{g}) \tag{6}$$

There is an alternative to the use of angular velocity, and that is used by the LEN algorithm, which works in terms of the velocity of the axis vector:

$$\mathbf{u} = \frac{d\hat{\mathbf{e}}}{dt} \tag{7}$$

In this algorithm, in order to apply the constraint that the length of the $\hat{\mathbf{e}}$ vector remains unity the calculation of an undetermined multiplier λ is needed in the way described in Ref. 6. In order to be completed, the algorithm needs the implementation of the linear velocities and positions (leapfrog algorithm, Eqs 8 and 9) and the calculation of the translational kinetic energy.

$$\mathbf{v}_{n+1/2} = \mathbf{v}_{n-1/2} + \mathbf{a}_n \delta t \tag{8}$$

$$\mathbf{x}_{n+1} = \mathbf{x}_n + \mathbf{v}_{n+1/2}\, \delta t \tag{9}$$

The time steps we used in the MD simulations ranged between 1 and 5 fs. The LEN algorithm behaved stably even with a time-step of 10 to 15 fs, but in this case it led to slightly different results for the diffusivities. The energy drift for the two gases and all models was lower than 0.2-0.4% during all MD runs. The test runs indicated that reliable self-diffusivities could be obtained from production runs of 30 to 180 ps.

The elaboration of molecular dynamics results towards the estimation of transport coefficients relies on Linear Response Theory (LRT) [15]. This provides the bridge between equilibrium time correlation functions and non-equilibrium response to weak perturbations. Through his regression hypothesis, namely that the relaxation of weak non-equilibrium disturbances follows the same laws as the regression of the spontaneous fluctuations at equilibrium, Onsager made the first attempt towards such a bridge before LRT formalized it [16]. LRT proves that the time integrals of autocorrelation functions are related to transport coefficients via relations known as Green-Kubo, of the following type

$$D_s = \frac{1}{d_o} \int_0^\infty dt \left\langle \frac{1}{N} \sum_{i=1}^N \mathbf{v}_i(t) \cdot \mathbf{v}_i(0) \right\rangle \tag{10}$$

Equation 10 relates the self-diffusivity D_s, averaged over a d_o-dimensional space over all the N molecules of the system, and the time integral of the autocorrelation function of the translational (center of mass) velocity $\mathbf{v}_i$ of the sorbate molecule i in MD simulations. An alternative, mathematically equivalent relation to eq. 10 is the Einstein equation, where

the average is taken over time for the mean squared displacement of the center of mass position vectors $\mathbf{r}_i$ of all the molecules in the system, i.e.

$$D_\mathrm{s} = \frac{1}{2d_o} \lim_{t\to\infty} \frac{d}{dt} \left\langle \frac{1}{N} \sum_{i=1}^{N} [\mathbf{r}_i(0) - \mathbf{r}_i(t)]^2 \right\rangle \tag{11}$$

Thus, the self-diffusivity D_s expresses the displacement of a tagged molecule among the remaining N-1 untagged molecules. It is the property measured using microscopic experimental techniques such as PFG-NMR, NMR-lifetime, and incoherent QENS.

According to LRT, the nonequilibrium macroscopic flux $\mathbf{J}$, which develops in response to a chemical potential gradient under steady-state conditions, can be written in terms of the time integral of the autocorrelation function of the instantaneous flux $\mathbf{j}(t)$ under equilibrium conditions (absence of chemical potential gradient), as follows [15]

$$\mathbf{J} = \langle\mathbf{j}\rangle_\mathrm{neq} = -\frac{V}{d_o} \int_0^\infty dt \, \langle \mathbf{j}(t) \cdot \mathbf{j}(0) \rangle \frac{\nabla\mu}{kT} \tag{12}$$

where V is the volume occupied by the system and the instantaneous flux is defined as

$$\mathbf{j}(t) = \frac{1}{V} \sum_{i=1}^{N} \mathbf{v}_i(t) \tag{13}$$

On the other hand, in macroscopic methods, such as measurement of the permeation rate, in a real membrane, molecules are considered to move under isothermal conditions with average velocity $\mathbf{v}$ subject to a driving force $\nabla\mu$ (chemical potential gradient of the penetrant in the membrane; $\mu = \mu^o + RT \ln f$ in terms of the fugacity f). So the flux (molecular current density) of fluid is defined through Fick's law [1, 32]

$$\mathbf{J} = -D_\mathrm{t}(c)\nabla c = -D_\mathrm{t}(c)c\frac{\partial \ln c}{\partial \ln f}\frac{\nabla\mu}{kT} \tag{14}$$

where D_t is the (in general concentration dependent) transport diffusivity; further manipulation of eq. 14 using the equation $\nabla\mu = kT\nabla f/f$, results in a concentration dependent Darken-like formula

$$D_\mathrm{t}(c) = D_0(c)\frac{\partial \ln f}{\partial \ln c} \tag{15}$$

from where the so called Darken or corrected diffusivity, D_0, is identified; its microscopic expression is given through the following relations [12, 34]

$$D_0 = \frac{1}{d_o N} \int_0^\infty dt \sum_{i=1}^N \sum_{j=1}^N \left\langle \mathbf{v}_i(t) \cdot \mathbf{v}_j(0) \right\rangle \tag{16a}$$

$$= D_{\mathrm{s}} + \frac{1}{d_o N} \int_0^\infty dt \sum_{i=1}^N \sum_{\substack{j=1 \\ j\neq i}}^N \left\langle \mathbf{v}_i(t) \cdot \mathbf{v}_j(0) \right\rangle \tag{16b}$$

Clearly, with $\mathbf{R}$ being the center-of-mass of the swarm of N molecules, eq 16a may equivalently be written in terms of the mean squared displacement of the center of mass position of the swarm, i.e.

$$D_0 = \frac{N}{2d_o} \lim_{t\to\infty} \frac{d}{dt} \left\langle [\mathbf{R}(0) - \mathbf{R}(t)]^2 \right\rangle \tag{17}$$

An alternative way of deriving the theoretical expression of D_0 in Fourier space in combination with Onsager's hypothesis, has been recently employed by Briels and co-workers [17, 18].

From eq. 16b it is clear that, as sorbate loading ρ tends to infinite dilution, cross-correlation functions between velocities of different molecules approach zero and the autocorrelation terms (self-diffusivity) predominate. Also, the sorption isotherm approaches the linear (Henry's law) regime. In this limit,

$$\lim_{\rho\to 0} D_0(\rho) = \lim_{\rho\to 0} D_{\mathrm{t}}(\rho) = \lim_{\rho\to 0} D_{\mathrm{s}}(\rho)$$

The statistical mechanics formulation of transport clearly indicates the physical character of each diffusion coefficient used in the study of sorbate flow. Thus, D_{s} is a pure kinetic property of individual molecules, D_0 is a pure kinetic property [34] that has a collective nature, since in addition to D_{s} it comprises the sum of the off-diagonal cross-correlation terms in the array of the velocity dot products (eq. 16b). On the other hand, D_{t}, which is also a collective property, embodies in addition the isotherm shape (eq 15), i.e, exhibits direct dependence on the sorption thermodynamics. All three properties are in general concentration dependent, exhibiting different concentration dependences.

An alternative to equilibrium MD for obtaining transport diffusivity is the utilization of non-equilibrium molecular dynamics techniques (NEMD), either beyond the linear response in the form of transient time correlation functions [20-22], which can be considered as the non-linear generalization of the Green-Kubo formulae, or within the linear response regime by calculating the sorbate flux caused by a (macroscopic) chemical potential gradient under transient [12, 23] or steady state flow conditions [12, 24-27] An extensive comparison of equilibrium MD, NEMD and hybrid methods for direct determination of transport diffusivity such as Dual Control Volume Grand

Canonical Molecular Dynamics under a constant chemical potential gradient [24-27], is found in Refs 26 and 27.

Sholl and co-workers [28, 29] have used standard equilibrium MD techniques for the prediction of non-equilibrium transport coefficients of various sorbates in silicalite-1 and carbon nanotubes [30]; also, Krishna and co-workers [29] have performed studies towards the prediction of transport diffusivities for pure sorbates and mixtures in zeolites on the basis of the Maxwell-Stefan theory. Sanborn and Snurr [31] have studied binary mixtures in faujasite using MD in order to obtain structural and transport properties of the system. Briels and co-workers [17, 18] have performed a study of transport diffusivity of Ar sorbed in AlPO4-5 based on equilibrium MD runs by employing the Green-Kubo approach in Fourier space; a wavevector-dependent diffusivity was obtained, allowing them to assess the correct linear-response result.

MD - Permeation. In a real membrane, in order to determine the thermodynamic behavior (sorption) of the fluid, a measured or predicted solubility coefficient S is defined, as

$$S = \frac{c}{f} \tag{18}$$

along with a local permeability coefficient, P_e, which provides information on the relationship between flux and driving force (fugacity gradient) locally at the considered point as a product of fundamental thermodynamic and dynamic properties, namely

$$P_e = D_0 S \tag{19}$$

Now the flux density can be written as

$$\mathbf{J} = -D_0 S \nabla f = -P_e \nabla f \tag{20}$$

hence,

$$D_t = D_0 S \frac{df}{dc} = D_0 \frac{c}{f} \frac{df}{dc} = D_0 \frac{\partial \ln f}{\partial \ln c} \tag{21}$$

and

$$D_t = P_e \frac{df}{dc} \tag{22}$$

In an actual steady-state permeation experiment an average permeability, $\overline{P}_e$, throughout the entire membrane is measured [33]. This is because the overall fugacity drop across the membrane of thickness L, $\Delta f = f_1 - f_2$, is known but not the local values of fugacity inside the membrane, as is the case in a simulation. To estimate $\overline{P}_e$, eq. 20 is integrated across the membrane using the Darken equation (eq. 21), namely [33]

$$\bar{P}_e \equiv \frac{J}{\Delta f / L} = -\frac{D_0}{\Delta f} \int_{c_1}^{c_2} \frac{\partial \ln f}{\partial \ln c} dc = -\frac{D_0}{\Delta f} \int_{f_1}^{f_2} \frac{c(f)}{f} df \qquad (23)$$

where $c(f)$ is the function expressing the adsorption isotherm of the adsorbate, as obtained from GCMC simulations. Average permeabilities computed in this way are compared to experimental values, with f_1 and f_2 being the fugacities on the high- and low-pressure sides of the membrane, respectively, used under the conditions of the experiment.

The above relations describe the methodology followed in the estimation of permeability from the corresponding diffusivities and isotherms computed through the simulations. The basic hypothesis being made is the validity of the Darken equation, as suggested by many authors [1, 12], and the assumption that the corrected diffusivity is independent of concentration; a detailed study of the latter dependence is made [34] in the next section.

Table 1 shows the computed single-component permeabilities in the form of ratios with respect to the macroscopic permeabilities measured by Yan, Davis and Gavalas [35] for supported (porous α-Al2O3) ZSM-5 membranes, for different sorbates. For the purpose of this comparison, it is more reasonable to use permeability ratios than absolute permeabilities, so that the influence of the morphological factors of the membrane on the adsorbate mobility can be factored out. As seen in the table, the calculated permeability ratios agree well with corresponding experimental values; they follow the order $CO_2 > CH_4 > N_2$, as has been measured by van de Broeke et al. [36] and Kusakabe et al. [37, 38]. Also, they are reasonably close to the permselectivity reported by Kusakabe et al. [37] for the binary mixture CO_2/N_2 ($\approx$ 5-7). It should be noted that permeability ratios measured on a given membrane practically coincide with the corresponding permeance ratios, i.e. the effect of the membrane thickness is largely factored out in taking the ratio.

Table I Predicted and experimental ratios in silicalite-1

Sorbates	P_e-ratios	Technique	Sorbent	T(K)
CH_4 / N_2	1.2	Supported Membrane Permeation[8]	ZSM-5 (M3)	303
CO_2 / CH_4	2.3	Supported Membrane Permeation[8]	ZSM-5 (M3)	303
CO_2 / N_2	2.8	Supported Membrane Permeation[8]	ZSM-5 (M3)	303
CH_4 / N_2	1.6	MD	Silicalite-1	300/298
CO_2 / CH_4	2.2	MD	Silicalite-1	303/300
CO_2 / N_2	3.4	MD	Silicalite-1	303/298

Although the predicted permeability ratios for the three pure gases through silicalite-1 under low occupancy conditions are in reasonable agreement with experiment,

the absolute values of predicted permeability are by a factor of 120 to 340 higher than the macroscopically measured experimental values [6]. These discrepancies in absolute values can be attributed to the following reasons: (i) In the present simulation analysis only the intracrystalline diffusion resistance has been taken into account in calculating the permeabilities, whereas in a macroscopic supported membrane experiment, or in an adsorption/desorption measurement, external mass transfer limitations may affect transport rates. (ii) Heat transfer is still a possibility and may reduce the overall permeation rate very significantly. Thus, transport rates from MD simulations, which are sensitive only to the resistance presented by intracrystalline diffusion in a perfect zeolite crystal under equilibrium conditions, tend to be considerably higher than macroscopically measured effective diffusivities, but quite close to diffusivities measured by the ''microscopic'' PFG-NMR and QENS methods. This is seen very characteristically in the results presented for the hydrocarbons methane, n-butane, and n-hexane in Ref. 6. (iii) Silicalite-1 has been modeled as a perfect, fully siliceous crystal. In macroscopic measurements, defects and aluminium (acid) sites are inevitably present, leading to a decrease in the mobility of sorbates. Intercrystalline boundaries, gel remaining between crystals, or nonidealities in the crystals have been proposed as sources of additional resistance [19]. Such defects are probably responsible for the fact that NMR-PFG and QENS diffusivities obtained in real silicalite-1 crystals for n-butane and n-hexane are by a factor of 3 or so lower than MD values [6].

The conclusion drawn for this atomistic study strongly supports the idea of modeling the transport hierarchically in the way introduced in the present chapter.

MD - QENS. The diffusion mechanism in the confined spaces of zeolite crystals depends basically on the concentration and the ratio of pore width over sorbate molecular size; when these sizes become comparable, the diffusing molecules remain subject to the strong potential field of the crystal at all times. Since this field is usually spatially inhomogeneous, transport occurs chiefly via random jumps of thermally activated molecules between "sites", or regions around potential minima, separated by energy barriers E_a; this behavior is frequently met inside the lattice of nanoporous zeolitic crystals, and referred to as intracrystalline diffusion process being subject to a temperature dependence of the Arrhenius type, i.e.

$$D = D_\infty \exp\left(-\frac{E_a}{RT} \right) \tag{24}$$

where R is the gas constant and T is absolute temperature.

In this section the first attempt towards a direct comparison of transport diffusivities from MD simulations and QENS experiments [34] is presented. From figure 1, the Arrhenius plots of transport diffusivities from coherent QENS and simulation for both sorbates at the same occupancy are seen to be in excellent agreement. Predicted activation energy values are very close to those experimentally determined.
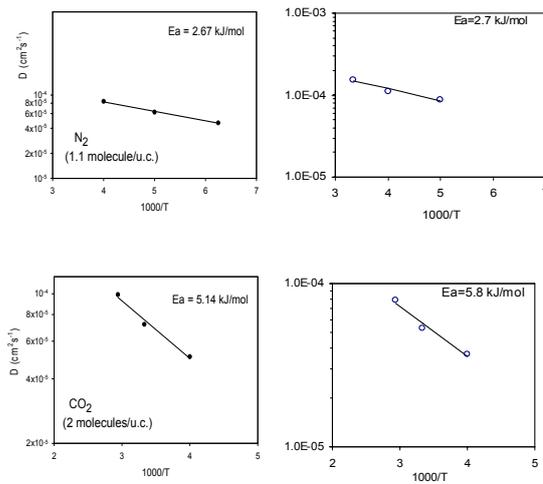
Fig. 1 Temperature variation (Arrhenius plots, see eq. 24) of the transport diffusivity of N_2 (top) and CO_2 (bottom) as obtained from coherent QENS measurements (left) and MD simulations (right) under the same conditions of loading. The activation energies extracted from the plots are given, for comparison.

The technique followed for the direct measurement of transport diffusivity via coherent QENS in figure 1, is due to Jobic et al. [39].

In figure 2, the results for the transport diffusivity measured directly from QENS measurements and our MD predictions for N_2 and CO_2, are presented; the corrected diffusivities in the QENS graphs have been produced via Darken factors obtained from the simulated isotherms. The increasing trend for transport diffusivity with occupancy for both gases is in excellent agreement with the QENS experiments, indicating a slightly concentration dependent D_0 over the sorbate loading range used in the experimental and simulation work. However, particular attention should be paid to the corrected diffusivity, which is largely free of thermodynamic influences, reflecting this way only the rate at which sorbate molecules escape from the potential minima due to the atomic structure of the sorbent.
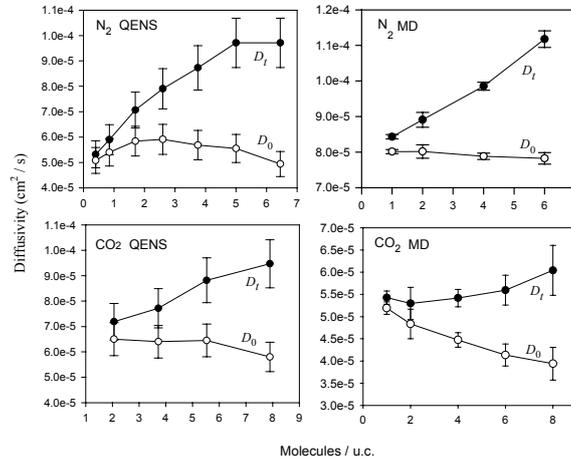
Fig. 2 Measured (QENS) and predicted (MD) transport (D_t) and corrected (D_0) diffusivities in silicalite-1 shown as functions of loading.

Figure 2 shows that the measured corrected diffusivity of CO_2 decreases as sorbate density increases, being in good agreement with the predictions from MD. In the case of N_2, the QENS measurements of D_0 exhibit a shallow maximum at a loading of roughly 2 molecules per unit cell; on the other hand, MD results show a rather occupancy-independent behavior of D_0 values. Small differences between predicted and measured values of D_t and D_0 can be attributed to the force fields used. It must be stressed here that no parameter adjustment was implemented at any point during calculations [34].

  Occupancy dependence of D_0. An attempt to investigate the dependence of the corrected diffusivity on the concentration of the sorbed phase has been made by Reed and Ehrlich [40], by invoking the Quasichemical mean field approximation [41, 42] in order to include the adsorbate-adsorbate energetics in a study of surface diffusion on a regular lattice of sites. This model was adapted to the current zeolite system through the mapping procedure discussed in detail in Ref. 34, thereby the following expression for the function $D_0(\theta)$ is derived,

$$D_0(\theta) = D_0(0) \left[\frac{\zeta + 1}{2 - 2\theta} \right]^{-z} \left[1 + \frac{\zeta - 1 + 2\theta}{2 - 2\theta} \exp(2w/kTz) \right]^{z-1} \qquad (25)$$

where θ is the fractional occupancy of the sorbate molecules in the zeolite, being considered as possessing a uniform lattice of sorption sites with coordination number z, and ζ is defined by the expression

$$\zeta = \{1 - 4\theta(1 - \theta)[1 - \exp(-2w/kTz)]\}^{1/2}$$

with w reflecting the pair interactions in the sorbed phase; k is the Boltzmann constant.
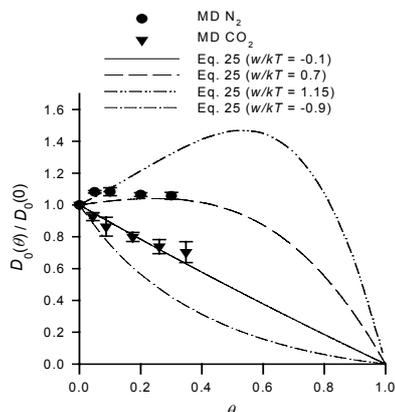
Fig. 3 Normalized corrected diffusivities from MD simulation and corresponding QC theoretical curves obtained from the Reed-Ehrlich model [40] for various pair interaction energy values.

Our simulation estimates for the diffusivities $D_0(\theta)$ for CO_2 and N_2 in silicalite-1, normalized by the corresponding $D_0(0)$ values, are presented in figure 3. In the same figure are given the $D_0(\theta)/D_0(0)$ curves obtained from the Reed-Ehrlich model, eq. 25, for the values of w/kT extracted from fitting the sorption thermodynamics [34]. Plots of eq. 25 for a higher and lower value of w/kT have also been included to display the overall behavior predicted by eq. 25. The model provides a satisfactory representation of the occupancy dependence of the corrected diffusivity. This supports the idea that the physical origin of the different $D_0(\theta)$ dependences seen in N_2/silicalite-1 at 200 K and CO_2/silicalite-1 at 300 K lies in the higher (more attractive) sorbate-sorbate interactions.

Clearly, use of a constant coordination number z is an oversimplification for a zeolite, as sorbate molecules do not arrange on a regular lattice inside such a system. At saturation, each of the three environments (straight channel, sinusoidal channel, and channel intersections) of silicalite-1 contains roughly two molecules; based on the spatial arrangement of these environments, one would estimate five neighbors for channel interiors and nine for channel intersections. In each case, one or two neighbors would be closer than the rest. The value z = 8 was found to give the best fit of the QC model to the isotherms among the values z = 2, 4, 6, 8, 10 tried.

Recently, Krishna et al. [50] have verified the loading dependence of the corrected diffusivity on the basis of the Stefan – Maxwell theory for diffusion by comparing MD and Kinetic Monte Carlo simulation results with the Reed-Ehrlich model.

2.1.2.2 Binary systems

Although the good agreement between the three microscopic techniques, PFG-NMR, QENS, and MD, is well established for pure sorbates [39, 43], relatively few

studies exist in the literature presenting direct comparisons between those techniques for mixed sorbates. A direct comparison between MD simulations and experimental self-diffusivities from PFG-NMR for a binary mixture of methane and tetrafluoromethane was made by Snurr and Kärger [44]. The reported self-diffusivities from the simulations were in good agreement with the experimental measurements. These authors observed that the diffusivities for both components, at constant total loading, decreased as the fraction of the larger and less mobile CF_4 increased. Also, Jost et al. [45, 46] have reported MD and pulsed field gradient NMR studies for the diffusion of methane-xenon mixtures over a wide range of loadings and compositions. This study showed that xenon diffusivity was unaffected by the presence of methane molecules at various concentrations. By varying the concentration of xenon, a monotonic decrease of the diffusivity of both species was observed.

Here, the first attempt to compare results obtained from molecular dynamics simulations and incoherent quasielastic neutron scattering experiments on a n-butane and methane mixture in silicalite-1 is presented, in order to elucidate the nature of intracrystalline motion probed by the two techniques [47, 48].

To connect the "theoretical" information, extracted from the MD simulation trajectories, with the experimental measurements, it is necessary to calculate the self-part of the van Hove correlation function using [49]

$$G_s(\mathbf{r},t) = \frac{1}{N}\sum_i \int \langle \delta(\mathbf{r}-\mathbf{r}'+\mathbf{R}_i(0))\delta(\mathbf{r}'-\mathbf{R}_i(t))\rangle d^3r' \tag{26}$$

The angular brackets denote a statistical or thermal average, and the sum is over all particles of a given type. The self-part of the Van Hove correlation function represents the conditional probability density for finding a particle at time t at a distance $\mathbf{r}$ from the position it occupied at time $t = 0$. As a next step, we have calculated the intermediate incoherent scattering function $I_s(\mathbf{Q},t)$, which is defined as the spatial Fourier transform of the self-part of the van Hove correlation function:

$$I_s(\mathbf{Q},t) = \int G_s(\mathbf{r},t)\exp(i\mathbf{Q}\cdot\mathbf{r})d^3r \tag{27}$$

where in QENS experiments, $\hbar\mathbf{Q}$ is the neutron momentum transfer. It is defined by $\boldsymbol{Q} = \boldsymbol{k} - \boldsymbol{k}_0$ where $\boldsymbol{k}$ and $\boldsymbol{k}_0$ are the scattered and incident wave vectors, respectively. Similarly, $\hbar\omega = E - E_0$ is the neutron energy transfer, with ω denoting the angular velocity. In the hydrodynamic limit ($\boldsymbol{Q}\rightarrow 0$, $t\rightarrow\infty$) where Fick's law describes diffusive motion, the orientationally averaged $I_s(\mathbf{Q},t)$ becomes:

$$I_s(\mathbf{Q},t) = \exp(-D_s Q^2 t) \tag{28}$$

with D_s being the self-diffusivity.

To check the consistency of our MD computations, we calculated the self-diffusivity from the intermediate scattering function $I_s(Q, t)$ in the limit of small Q and long times t, where eq. 28 holds.

Table II Self-diffusivity of CH_4 as obtained from MD simulations and from QENS experiments, for CH_4 loading being held constant at 4 molecules per unit cell; T=200 K.

n-C_4H_{10} loading (molec./u.c.)	D_s^{CH4} – MD (10^{-5} cm^2/sec)	D_s^{CH4} – QENS (10^{-5} cm^2/sec)
0	3.9	2.2
2.5	2.4	1.4
5.0	0.93	0.5
7.5	0.18	0.12

Direct comparisons of the MD predictions with the QENS measurements for the methane self-diffusivity as a function of the n-butane loading are shown in Table II. The methane D_s decreases, by significantly increasing the loading of n-butane. As the n-butane loading rises from 0 to 7.5 molecules per unit cell, both computed and measured D_s falls by a factor of 20. This is because the strongly adsorbed butane molecules effectively block the passage of methane molecules through the channels.

Table III shows the methane self-diffusivity as a function of methane loading. It is seen that D_s falls by a factor of 9 in QENS and by a factor of 4 in MD as methane loading increases from 2 to 10 molecules per unit cell. D_s decreases as loading increases for both species. The agreement between the predicted diffusivities from simulation and the measured ones from the experiment is excellent, although the values obtained from MD are somewhat higher than the QENS measurements. This is explainable on the basis that the energetics of the simulated zeolite model correspond to a perfect rigid crystal lattice, whereas in the real medium the existence of defects and impurities could reduce the molecular mobility.

Table III Self-diffusivity of CH_4 as obtained from MD simulations and from QENS experiments, for n-C_4H_{10} loading being held constant at 4 molecules per unit cell; T=200 K.

CH_4 loading (molec./u.c.)	D_s^{CH4} – MD (10^{-5} cm^2/sec)	D_s^{CH4} – QENS (10^{-5} cm^2/sec)
2	1.8	1.3
4	1.4	1.1
6	1.0	0.58
8	0.8	0.27
10	0.5	0.14

The discrepancy observed at the higher methane loadings can be attributed to the larger error associated with the neutron scattering experiments at low diffusivity values.

An interesting aspect on the theoretical treatment of diffusion in zeolites was given by Krishna [51], who verified directly the Stefan-Maxwell formulation [1] for mixture diffusion, by exploiting previous MD data [44, 46, 47] for diffusion of mixtures in silicalite-1, and showed that the mixture transport behavior can be predicted from the corrected diffusivities of the pure components at infinite dilution.

2.2 Mesoscopic scale

In the previous section the mass transport phenomena under investigation were confined in the intracrystalline region of zeolites where microscopic techniques for probing diffusivity such as molecular dynamics simulations and quasielastic neutron scattering measurements are directly applicable. Nevertheless, transport in membranes, as discussed for example in Table I or in catalytic beds, clearly comprises the intercrystalline space, where intermolecular and interfacial collisions contribute to the overall flow. Diffusion at restrictions resulting from intracrystalline transport barriers in MFI-type crystals due to intersections and intergrowth sections between the elementary structural crystal units, have been studied experimentally by using Pulsed Field Gradient Nuclear Magnetic Resonance (PFG NMR), Interference Microscopy, and Monte Carlo simulation for methane, n-butane and i-butane diffusion, by Kärger and coworkers [52, 53].

In the next section, mesoscopic predictions from kinetic Monte Carlo simulations of ethane in a bed of zeolite NaX are compared with PFG NMR measurements of long range diffusivity in the same system.

2.2.1 Model of NaX bed

A digitally reconstructed model of a real bed of NaX has been developed on the basis of the experimental data concerning the edge length distribution $(\overline{\ell} = 30 \ \mu\mathrm{m})$ and the shape of the crystal (perfect octahedron) used in Refs 54, 55. For the reconstruction of porous media consisting of particles of simple geometric shapes, as in the case of the octahedral crystal particles in a bed of NaX zeolite, a new computational method has been developed. For the modeling of the octahedra we have applied continuous potentials between spheres of similar volume in fcc ordering which fill up the sides of each octahedron. The representation of the particles is being improved by progressively increasing the number of spheres N_s until a sufficiently high resolution is achieved, according to the formula:

$$N_s = 4G^2 + 2 \tag{29}$$

Following this procedure, beds of octahedra are generated with prescribed porosity given by the experimental data. The volume V_{obj} of one coarse grained octahedron (object) in the reconstructed medium is then given by the relation:

$$V_{obj}=V_{oct}+NV_{sph} - [\ 6v_{ap} + 12(G-1)v_{ed} + 4(G-1)(G-2)v_{fa}\ ] \qquad (30)$$

where V_{oct} is the geometric volume of octahedron and v_{ap}, v_{ed}, and v_{fa} are the volumes of the part of sphere lying inside the octahedron when the sphere lies with its center on an apex, edge and face respectively. As the number of generations increases, $V_{sph} \rightarrow 0$ and consequently $V_{obj} \cong V_{oct}$.
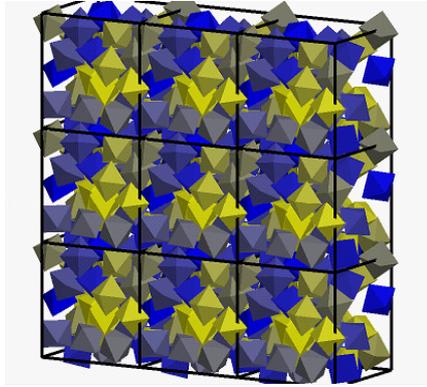
Fig. 4   Reconstructed bed of NaX crystals of porosity $\phi = 0.6$, periodically repeated in 3D space.

At each generation G, the medium configuration is subjected to a multi-parametric energy minimization process with respect to the positions and orientations of the crystallites using the quasi-Newton based algorithm of Broyden-Fletcher-Goldfarb-Shanno (BFGS). Minimization proceeds until the system is well-relaxed, satisfying the conditions of detailed mechanical equilibrium (Fig. 4). The final relaxed structure at a given G is used as initial configuration for the next generation. This procedure was repeated up to $G = 19$, our highest generation examined, which eventually was accepted as the representation of the medium.

2.2.2 Diffusion
Kinetic Monte Carlo. The method is used for the calculation of the self-diffusivity of ethane in the medium of NaX crystals (Fig. 4) by computing the mean-square displacement of a fixed number of molecules N_s in the bed. The molecules are assumed to travel with the mean thermal speed, $\bar{u}$, given by the Maxwell velocity distribution [56]. A random change in the direction of motion occurs after any molecule-molecule collision. Upon collision with a crystal surface, a new directory is selected according to the cosine law [60]. Random trajectories are generated in the void space of the medium in such a way so that in the bulk gas the lengths l between successive collisions follow an

exponential distribution expected from the Poisson process character of intermolecular collisions [56]:

$$\langle l \rangle f(l) = \exp(-l/\langle l \rangle) \tag{31}$$

where $f(l)$ is the conditional probability of having a collision-free trajectory length between l and $l + dl$ with a mean value of l being denoted by $\langle l \rangle$. In the bulk gas phase, $\langle l \rangle$ is molecular mean free path $\lambda = kT/p\sigma^2\pi\sqrt{2}$. In the Knudsen regime, $\langle l \rangle$, the mean intercept length with crystallite walls, can be considered as an effective yardstick of the porous matrix [57]; the calculated value for the bed of fig. 4 is 71.4 μm, about by a factor of two higher than the experimentally measured mean edge length of the NaX octahedral crystal, 30 μm. This finding indicates that realistic crystal geometries as well as the existence of intercrystalline potential fields can give rise to a different packing than the ones expected from ideal porous structures studied in previous works, e.g. in digitized media [58] or sphere packings [57, 59].

The trajectory lengths of the molecules in the Knudsen regime are interrupted merely by the crystal surfaces. For the porosity under consideration, $\phi = 0.6$, the computed ratio of the two first moments of $f(l)$ is found to be $\dfrac{\langle l^2 \rangle}{2\langle l \rangle^2} = 0.866$; the same ratio would be equal to 1 for a strictly Poisson process. This finding indicates that the exponential distribution (eq. 31) is progressively invalidated as the participation of the molecular collisions with the wall increases.

In figure 5, the diffusivity of ethane is presented over a wide range of mean free path, from the Knudsen to the molecular regime. In the transition regime, the computed diffusivities satisfy the Bosanquet relationship [60]:

$$\frac{1}{D_s} = \frac{1}{D_K} + \frac{1}{D_B} \tag{32}$$

where D_K and D_B are the two limiting D_s values in the bed under pure Knudsen and molecular diffusion conditions in the bulk regime, respectively.
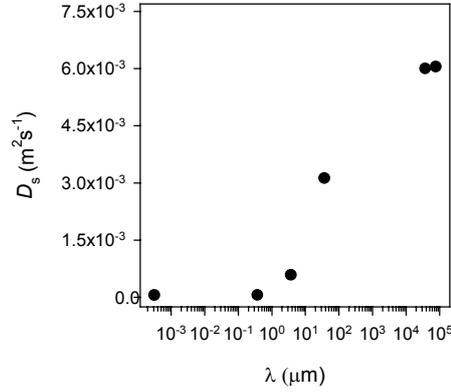
Fig. 5 Transition of D_s from molecular to Knudsen diffusion regime as a function of mean free path λ for C_2H_6 in a bed of NaX crystals at 298 K.

Defining the tortuosity factors η_K and η_B for the two mentioned limits as follows

$$\eta_K = \frac{D_{0K}}{D_K} \qquad \eta_B = \frac{D_{0B}}{D_B}$$

where D_{0K} and D_{0B} are the reference diffusivities in the Knudsen and bulk regimes respectively, given by the formulae

$$D_{0K} = \frac{1}{3}\overline{u}\langle l \rangle \quad \text{and} \quad D_{0B} = \frac{1}{3}\overline{u}\lambda \,,$$

we calculated the values $\eta_K = 1.81$ and $\eta_B = 1.05$. This difference between the two tortuosity factors in the Knudsen and bulk regime is in agreement with the measured factors from PGF NMR by Kärger and coworkers [54, 55]. The much lower deviation from unity of the tortuosity in the bulk regime is consistent with previous simulation studies in simple pore matrices for so high porosity values [57-59].

The Derjaguin [61] formulation for D_{0K} explicitly takes into account the nonexponential nature of the distribution $f(l)$ in the Knudsen regime; assuming also that no correlation exists between consecutive trajectory lengths and that trajectory orientations and lengths are mutually independent, Derjaguin's approach leads to

$$D_{0K} = \frac{1}{3}\overline{u}\langle l \rangle \left[\frac{\langle l^2 \rangle}{2\langle l \rangle^2} - \beta \right] \tag{33}$$

where $\beta = -\sum_{j=2}^{\infty} \langle \cos \gamma_{ij} \rangle$, and γ_{ij} denotes the angle between trajectory lengths l_i and l_j.

Now, the Knudsen tortuosity factor obtained from the simulations using eq. 33 becomes $\eta_K = 1.02$ practically identical to that for bulk diffusion. It is obvious that the ratio $\langle l^2 \rangle / 2 \langle l \rangle^2$ reflects the pore shape of the medium, i.e. the local interfacial geometry; the angular factor β, on the other hand, depends on the model used in order to describe molecular collision with the solid surface in the bed. In this work as mentioned above the cosine law [60] was used for reflection from surfaces; our computed value is $\beta = 0.3051$ versus the theoretical value of 14/3 ($\cong 0.3077$) obtained by Derjaguin in a medium of randomly placed spheres.

3. Conclusion

A multiscale computer simulation study of diffusion of pure gases and mixtures in a representative kind of nanoporous materials, zeolites, was carried out. Self- and transport diffusivity predicted by molecular dynamics at the atomistic scale are in excellent agreement with microscopic experiments for CO_2 and N_2 in silicalite-1 crystal. The comparison of predicted and measured transport diffusivities interpreted in the light of a simple quasichemical theory, gave an explanation for the physical origin of the sorbate loading dependence of corrected and hence of the transport diffusivity. Furthermore, permeability ratios for various pairs of pure sorbates calculated from simulation of transport in single crystals, showed very good agreement with the corresponding ratios measured in actual silicalite-1 membranes.

The results of kinetic Monte Carlo simulations for the long-range diffusivity of ethane in a bed of zeolite NaX, confirmed the evidence for different apparent tortuosity factors in the Knudsen and bulk regimes, which was first observed via PFG NMR measurements in the same system; further analysis of the kinetic Monte Carlo simulation results revealed that the latter difference can be attributed to the dependence of the molecular paths on the geometry of the particles and the porosity of the zeolitic bed. Involving an alternative definition of Knudsen diffusivity by Derjaguin, in which the shape of actual long-range definition paths is taken into account, one obtains identical tortuosity factors for the Knudsen and molecular regimes.

References

1.   Kärger J. and Ruthven D. M. *Diffusion in Zeolites and Other Microporous Solids* Wiley-Interscience, New York ,1992

2.   Bell A. T., Maginn E. J. and Theodorou D. N. in *Handbook of Heterogeneous Catalysis*, Vol. 3, p. 1165, Ertl E.G., Knozinger H. and Weitkamp J.; Eds, Wiley-VCH: Weinheim, Germany (1997)

3.   Theodorou D. N., Snurr R. Q. and Bell, A. T. in *Comprehensive Supramolecular Chemistry*, Vol. 7, p. 507, Alberti G. and Bein T. Eds, Pergamon (1999)

4.   van de Graaf B., Njo S. L. and Smirnov K. S. in *Reviws in Computational Chemistry*, Vol. 14, p. 137, Lipkowitz K. B. and Boyd D. B. Eds, Wiley-VCH: John Wiley and Sons, Inc., New York (2000)

5.   Mentzen B. F. and Sacerdotte-Perronnet M., *Mat. Res. Bull.*, 28, 1017 (1993)

6.   Makrodimitris K., Papadopoulos G. K., and Theodorou D. N., *J. Phys. Chem. B*, 105, 777 (2001)

7.   Lonsinger S. R., Chakraborty S. R., Theodorou D. N. *Catal. Letters* , **11**, 209 (1991); Cook S. J., Chakraborty A. K., Bell A.T., Theodorou, D. N. *J. Phys. Chem.*, **97**, 6679 (1993)

8.   Snurr, R.Q.; Bell, A. T.; Theodorou D.N. J. Phys. Chem, 97, 13742 (1993)

9.   June R. L., Bell A. T., Theodorou D. N., *J. Phys. Chem*, 94, 1508 (1990)

10.   Watanabe K., Austin N., Stapleton M. R., *Mol. Simul.*, 15, 197 (1995)

11.   June L. R., Bell A. T., Theodorou D. N., *J. Phys. Chem.*, 96, 1051 (1992)

12.   Maginn E. J., Bell A. T., Theodorou D. N., *J. Phys. Chem.*, 97, 4173 (1993)

13.   Mazur Al., *J. Comput. Phys.*, 93, 171 (1997)

14.   Fincham D., *Mol. Simul.*, 11, 79 (1993)

15.   Hansen J. P., McDonald I. R., *Theory of simple liquids*, Academic Press, London, 1986

16.   L. Onsager, *Phys. Rev.* 37, 405 (1931); *ibid*. 38, 2265 (1931)

17.   Hoogenboom, J. P.; Tepper, H. L.; van der Vegt, N. F. A. Briels, W. J. *J. Chem. Phys.*, 2000, 113, 6875

18.   Tepper, H. L.; Briels, W. J. *ibid*., 116, 9464 (2002)

19.   Graaf J. M.; Kapteijn F.; Moulijn, *J. Microporous and Mesoporous Materials*, 35-36, 267 (2000)

20.   Visscher, V. M. *Phys. Rev. A*, 10, 246 (1974)

21.   Evans, D. J.; Morriss, G. P. *Phys. Rev. A*., 38, 4142 (1988)

22.   Petravic, J.; Evans, D. J. *Phys. Rev. Lett*., 78, 1199 (1997)

23.   Arya, G.; Maginn, E. J.; Chang, H.-C. *J. Chem. Phys*., 113, 2079 (2000)

24.   Heffelfinger, G. S.; van Swol, F. *J. Chem. Phys*., 100, 7548 (1994)

25.   MacElroy, *J. Chem. Phys*., 101, 5274 (1994)

26.   Arya, G.; Chang, H.-C.; Maginn, E. J. *J. Chem. Phys*., 115, 8112 (2001)

27.   Papadopoulos, G. K., *Molec. Simulation*, 31, 57 (2005)

28.   Skoulidas, A. I.; Sholl, D. S. J. Phys. Chem B., 106, 5058 (2002)

29.   Skoulidas, A. I.; Sholl, D. S.; Krishna, R. Langmuir , 19, 7977 (2003)

30.   Skoulidas A. I., Ackerman D. M.; Johnson J. K.; Sholl D. S. *Phys. Rev. Lett*., 89, 185901 (2002)

31.   Sanborn, M. J.; Snurr, R. Q. *Sep. Purif. Technol*., 20, 1 (2000)

32.   Papadopoulos G. K., Petropoulos J. H. *J. Chem. Soc*., *Faraday Trans*., 92, 3217 (1996)

33.   Papadopoulos G. K., *J. Chem. Phys*., 114, 8139 (2001)

34 .   Papadopoulos G. K., Jobic H., Theodorou D. N.,   *J. Phys. Chem. B*, 108, 12748 (2004)

35.   Yan Y., Davis M. E., Gavalas G. R., *Ind. Eng. Chem. Res*., 34, 1652 (1995)

36. van den Broeke, L.J.P.; Bakker, W.J.W.; Kaptein F.; Moulijn, J.A. *Chem. Eng. Sci.*, 54, 245 (1999)

37.   Kusakabe, K.; Yoneshige, S.; Murata, A.; Morooka, S. *J. Membrane Sci*., 116, 39 (1996)

38.   Kusakabe K., Sakamoto S., Toshiyuki S., Morooka S., *Separation and Purification Technology*, 16, 139 (1999)

39.   Jobic H.; Kärger J.; Bee, M. *Phys. Rev. Lett*., 82, 4260 (1999)

40.   Reed D. A., Ehrlich G., *Surface Sci.*, 102, 588 (1981)

41.   Fowler, R. and Guggenheim, E. A. *Statistical Thermodynamics*, University Press, Cambridge, 1949; p. 421

42.   Bethe, A. *Proc. Roy. Soc. A*, 150, 552 (1935)

43.   Jobic H., Ernst H., Heink W., Kärger J., Tuel A., Bee M., *Micropor. Mesopor. Mater.*, 26, 67 (1998)

44.   Snurr R. Q., Kärger J., *J. Phys. Chem. B*, 101, 6469 (1997)

45.   Jost, S.; Fritzsche, S.; Haberlandt, R. *Chem. Phys. Lett.*, 219, 385 (1997)

46.   Jost, S.; Bar, N. K.; Fritzsche, S.; Haberlandt, R.; Kärger, J. *J. Phys. Chem. B.*, 102, 6375 (1998)

47.   Gergidis L. N., Theodorou D. N., *J. Phys. Chem. B*, 103, 3380 (1999)

48.   Gergidis G. N., Theodorou D. N., Jobic H., J. Phys. Chem. B, 104, 5541 (2000)

49.   Gaub M., Fritzsche S., Haberlandt R., Theodorou D. N., *J. Phys. Chem. B*, 103, 4721 (1999)

50.   Krishna R., Paschek D., Baur R., *Microporous Mesoporous Mat.*, 76, 233 (2004)

51.   Krishna R., *Chem. Eng. J.*, 84, 207 (2001)

52.   Vasenkov S., Böhlmann W., Galvosas P., Geier O., Liu H., Kärger J., *J. Phys. Chem. B.*, 105, 5922 (2001)

53.   Geier O., Vasenkov S., Lehmann E., Kärger J., Schemmert U., Rakoczy R., Weitkamp J., *J. Phys. Chem. B.*, 105, 5922 (2001)

54.   Geier O., Vasenkov S., Kärger J., *J. Chem.. Phys.*, 117, 1935 (2002)

55.   Vasenkov S., Geier O., Kärger J., Eur. Phys. J. E., 12, s35 (2003)

56.   Kennard H., *Kinetic theory of gases*, McGraw-Hill, New York, 1938

57.   Levitz P., *J. Phys. Chem.*, 97, 3813 (1993)

58.   Burganos V. N., *J. Chem. Phys.*, 109, 6772 (1998)

59.   Zalc J. M., Reyes S. C., Iglesia E., *Chem. Eng. Sci.*, 59, 2947 (2004)

60.   Cunningham R. E., Williams R. J. J., *Diffusion in Gases and Porous media*, Plenum Press, New York, 1980

61.   Derjaguin B., *C. R. Acad. Sci. URSS*, 7, 623 (1946)